



HAL
open science

The influence of disks deformation on the stability analysis of an aircraft braking system

Xavier Fagan, Jean-Jacques Sinou, Sébastien Besset, Louis Jézéquel,
Abdelbasset Hamdi

► **To cite this version:**

Xavier Fagan, Jean-Jacques Sinou, Sébastien Besset, Louis Jézéquel, Abdelbasset Hamdi. The influence of disks deformation on the stability analysis of an aircraft braking system. *Archive of Applied Mechanics*, 2024, 95 (1), pp.13. 10.1007/s00419-024-02715-1 . hal-04813778

HAL Id: hal-04813778

<https://hal.science/hal-04813778v1>

Submitted on 2 Dec 2024

HAL is a multi-disciplinary open access archive for the deposit and dissemination of scientific research documents, whether they are published or not. The documents may come from teaching and research institutions in France or abroad, or from public or private research centers.

L'archive ouverte pluridisciplinaire **HAL**, est destinée au dépôt et à la diffusion de documents scientifiques de niveau recherche, publiés ou non, émanant des établissements d'enseignement et de recherche français ou étrangers, des laboratoires publics ou privés.



Distributed under a Creative Commons Attribution - NonCommercial - NoDerivatives 4.0 International License



ORIGINAL

X. Fagan · J.-J. Sinou · S. Besset · L. Jézéquel · A. Hamdi

The influence of disks deformation on the stability analysis of an aircraft braking system

Received: 16 July 2024 / Accepted: 10 October 2024
© The Author(s) 2024

Abstract Friction-induced vibration emanating from aircraft braking system is a key issue in the design phase, due to the significant damage it can cause to the brake structure. Although the problem of unstable vibrations in aircraft braking systems has been studied by a number of researchers, the suitability of the mechanical modeling strategy for predicting instabilities remains an open problem. The need for relevant numerical models is therefore essential in order to be as predictive as possible during the design phase. Preliminary studies must therefore be carried out to validate or invalidate the modeling hypotheses traditionally used. Indeed the stability analysis of an aircraft braking system is performed in order to study a low-frequency instability. An industrial model is used, hence reducing the number of degrees of freedom (DoF) is of utmost importance in order to have reasonable computation times. When studying low-frequency phenomena, this can be achieved by neglecting the deformations of the disks. However, no current study has shown that this hypothesis is realistic. So the aim of this paper is to assess the effect of the rigidity hypothesis on the results predicted by the stability analysis. In order to do so, the stability analysis results of a model with rigid disks and one with non-rigid disks are compared, with a particular attention on the main instability phenomenon. It is found that considering rigid disks has a very limited influence on the frequency of the low-frequency eigenmodes, but it over-predicts the real part of the unstable eigenmode. Besides, a component mode synthesis (CMS) technique is shown to reduce significantly the size of the non-rigid disks model while ensuring a satisfying precision regarding eigenmodes prediction.

Keywords Mode-coupling instability · Stability analysis · Component mode synthesis · Structural deformation

1 Introduction

Friction-induced instabilities affect braking systems in a large spectrum of vehicles: studies have dealt with this topic in bicycles [1], cars [2–5], trains [6–13] or aircraft [14, 15]. Such issues have been known for decennia, but their prediction and mitigation is still a challenge for industries [16–18]. Several theories have been used to explain the physical origins of friction-induced vibrations [19] and extensive comprehensive reviews on mechanisms of the brake instabilities and friction-induced vibration are available [2, 20–23].

X. Fagan · J.-J. Sinou · S. Besset · L. Jézéquel
Laboratoire de Tribologie et Dynamique des Systèmes, UMR CNRS 5513, École Centrale de Lyon, 36 avenue Guy de Collongue, 69134 Écully, France
E-mail: jean-jacques.sinou@ec-lyon.fr

X. Fagan · A. Hamdi
Safran Landing Systems, Inovel Parc Sud 7 rue Général Valérie André, 78140 Vélizy-Villacoublay, France

Two complementary approaches are used to predict the severity of friction-induced instabilities: the first step is to perform a stability analysis. This is achieved by linearizing the system around a static equilibrium point and then computing the eigenmodes and eigenfrequencies. The real part of the eigenmodes is studied with Complex Eigenvalue Analysis (CEA): this tool is largely used in the industry, automotive being one example [24]. It is quite fast to compute and provides useful insight into the eigenmodes of the system. Sometimes this is not sufficient though, as it has been showed that in some cases the predictions of the CEA do not match the behavior of the real system, in particular when several instabilities are taken into account [25,26]. Besides, stability analyses only provide local information about the bifurcation point. It is often important to know not only whether an instability will manifest, but also the vibration levels that the structure will be exposed to. Other methods appeared in order to compensate for the downsides of the CEA: for instance, nonlinear approaches such as the Harmonic Balance Method (HBM) [27] and the shooting method [12] allow to determine the steady-state solution. The nonlinear time simulation provides the transient-state solution as well and direct access to vibration levels [28]. Those methods take into account nonlinearities and are valid even after the bifurcation point is reached. The main downside is the computation time required, significantly higher than for a CEA [27].

Industrial models are interesting because they can deal with complex phenomena and precisely describe the behavior of a given system. In order to do so, a high number of degrees of freedom (DoF) are considered. The main difficulty is to reduce the size of the model while keeping a satisfying precision on the phenomena under study. When dealing with an industrial model, the first step is usually to apply a reduction method to the internal modes of the structures. The most common ones are the Craig-Bampton [29] (fix-interface modes) and the Craig-McNeal [30] (free-interface modes) methods. For the reduction of the interface modes, other techniques can be applied, for instance hyper-reduction [31] or Double Modal Synthesis [32,33]. Once the simulation time for one set of parameters is satisfactory, it is possible to pursue with more in-depth study of friction-induced vibration and even to improve the system through optimization [34].

Aircraft braking systems are similar to disk brakes found in the automotive industry, the main difference being that several disks are stacked together, hence multiple disk-on-disk contact surfaces appear. Dealing with aircraft braking systems, the main unstable modes appear at low frequencies (in general a few hundred hertz). The disks deformation is very limited in this frequency range, so it is possible to simplify the model by considering rigid disks. This hypothesis does not prevent the instabilities from appearing in phenomenological models [35,36]. Besides, in some contexts considering rigid or deformable bodies has a remarkable impact on either the results provided by the model or its computation time [37,38].

The paper deals with the issue of model size reduction toward simulating friction-induced instabilities, with an application to an industrial model of an aircraft braking system. In particular, it describes the effects of the rigidity hypothesis on the stability analysis of the braking system model. It will assess whether the hypothesis provides a satisfying model for stability analysis by comparing the performance (i.e., precision and model size) for a rigid-disk model and for a non-rigid-disk model. On the other hand, taking into account the disks deformation requires to increase the size of the model, which will in turn increase the computation time required. Therefore, this paper uses a Component Mode Synthesis (CMS) method in order to analyze whether it can be combined with the non-rigid model and improve its computation time.

First of all, the industrial braking system is described: the principle of braking and the main subsystems are listed, then the main instability affecting the system is introduced. Two models are then described and compared: one with rigid disks model and one with non-rigid disks. Their contact formulations are compared and the results obtained through stability analysis are shown. After assessing the improvement obtained through considering disks deformation, the results obtained through CMS are described in order to assess the efficiency of this reduction method.

2 Model of the braking system

2.1 Industrial model and context

Figure 1 shows the Finite Element model of an aircraft braking system. It is made of a stacking of rotors and stators. Several pistons are installed on a piston housing and they control the braking through the contact pressure. The disks are guided in order to allow only for axial translation between the disks and the structure. The rotors are guided by the wheel rim, while the stators are guided by the axle. Before the braking sequence is started, the disks move at different rotating speeds and they are not in contact. Once the pressure in the piston housing raises, pistons make contact with the first disk and push the heat sink (assembly of the rotors

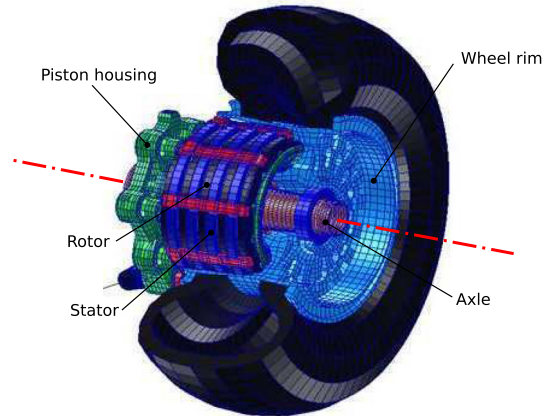


Fig. 1 Finite Element model of an aircraft braking system with its rotation axis

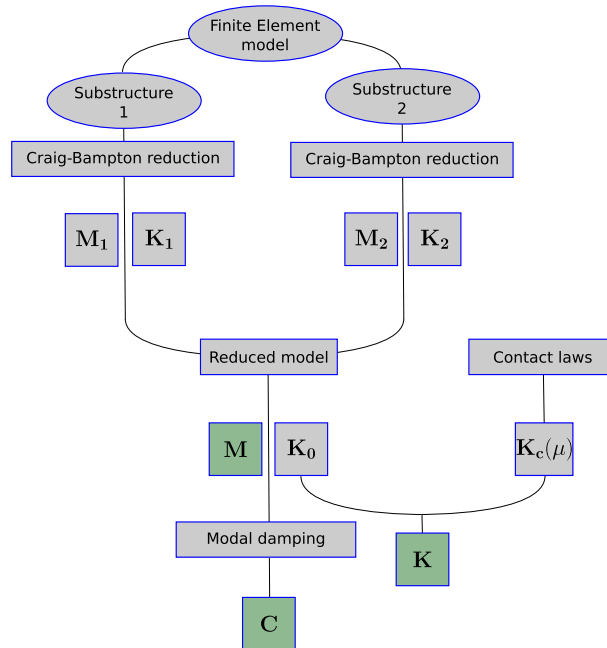


Fig. 2 Framework for obtaining the reduced model

and the stators) together. Friction forces appear and a braking torque is generated, allowing the plane to reduce its speed.

During the development of a new braking system, a series of tests is performed in order to monitor its behavior thanks to several accelerometers. Vibrations exceeding the requirements are observed on some occasions, and after investigation the cause is often found to be the presence of a mode-coupling instability [15,39]. The one studied in this paper is called whirl and is characterized by a low frequency, around 200 Hz. It will be defined by f_0 in the rest of the paper. Displacement-wise, whirl is an out-of-plane oscillation of the heat sink and the piston housing. An illustration of this eigenmode is provided in Annex A. In the context of braking systems, whirl can spur high-intensity vibrations. Such levels lead to disks wear and can jeopardize the structural integrity of the landing gear. It is then fundamental to be able to control this instability and to limit the vibration levels associated to it. This requires to be able to predict the behavior of a given braking system depending on its architecture and on the braking conditions.

A complete aircraft braking system model is defined by several millions of DoF. At the same time, the most important phenomena are generally located in the low-frequency range. Hence, it is possible to simplify the behavior of the model while being able to reproduce the required instabilities. Figure 2 illustrates the method

employed to obtain the reduced model. First, the braking system is separated into two substructures: each of them is then reduced through a Craig-Bampton method and their convergence is verified for the frequency range of interest. The following step is to recombine the two substructures using their boundary conditions.

2.2 Equation of motion of the braking system

The equation of motion of the system is written as follows:

$$\mathbf{M}\ddot{\mathbf{x}} + \mathbf{C}\dot{\mathbf{x}} + \mathbf{K}\mathbf{x} = \mathbf{f}_{\text{ext}} + \mathbf{f}_{\text{NL}}(\mathbf{x}) \quad (1)$$

The matrices \mathbf{M} and \mathbf{K} are the mass and stiffness matrices of the braking system. The forces applied to the system are divided into two entities. \mathbf{f}_{ext} corresponds to the external forces on every DoF of the system: in the paper, the weight of the plane and the pressure forces coming from the pistons are taken into account. The nonlinear forces are described by $\mathbf{f}_{\text{NL}}(\mathbf{x})$. The influence of the rotation of the wheel is neglected here, hence no gyroscopic terms appear in Eq. 1. The stiffness matrix is composed of a structural term \mathbf{K}_0 , directly extracted from the Finite Element model, and a term depending on the contact laws between the disks \mathbf{K}_c .

$$\mathbf{K}(\mu) = \mathbf{K}_0 + \mathbf{K}_c(\mu) \quad (2)$$

The damping matrix \mathbf{C} is defined in the modal basis of the undamped system such as:

$$C_{ii}^0 = 2\omega_{i,0}\xi_i \quad (3)$$

Where $\omega_{i,0}$ defines the angular frequency of the i^{th} mode and ξ_i corresponds to the associated modal damping ratio. Identifying the modal damping of a mechanical system is a very difficult and delicate task, but for the sake of simplicity, here a constant modal damping ratio of 3% is considered for all eigenmodes. A transformation is then required in order to write the damping matrix in the same basis as the mass and the stiffness ones.

In order to operate such transformation, let us consider the undamped and frictionless system:

$$\mathbf{M}\ddot{\mathbf{x}} + \mathbf{K}(\mu = 0)\mathbf{x} = \mathbf{0} \quad (4)$$

Both matrices are real and symmetrical, hence they are diagonalizable. By scaling the eigenvectors with respect to the mass matrix, we obtain:

$$\Phi^T \mathbf{M} \Phi = \mathbf{I} \quad (5)$$

Where \mathbf{I} corresponds to the identity matrix. The modal matrix Φ is obtained by solving the eigenvalue problem of the system's equation of motion. The damping matrix verifies the following equation:

$$\Phi^T \mathbf{C} \Phi = \mathbf{C}^0 \quad (6)$$

\mathbf{C}^0 is a diagonal matrix which terms are given by Eq. 3. Hence, it is possible to obtain an expression for the damping matrix in the basis of the DoF of the model:

$$\mathbf{C} = \mathbf{M} \Phi \mathbf{C}^0 \Phi^T \mathbf{M}^T \quad (7)$$

By defining the damping matrix in such way, the real part of each eigenmode is shifted by a value proportional to its eigenfrequency:

$$r_i(\xi_i) = r_i(0) - \omega_i \xi_i \quad (8)$$

2.3 Stability analysis

Here the main steps required to perform a stability analysis are summarized.

Under the hypothesis that Eq. 1 admits a sliding equilibrium point \mathbf{x}_{eq} , it verifies:

$$\mathbf{K}\mathbf{x}_{\text{eq}} = \mathbf{f}_{\text{ext}} + \mathbf{f}_{\text{NL}}(\mathbf{x}_{\text{eq}}) \quad (9)$$

A solution can easily be found in the linear case. If nonlinear forces are considered, methods such as Newton–Raphson are used to evaluate the solution.

Once an equilibrium point is calculated, a point $\bar{\mathbf{x}}$ in its vicinity can be defined as follows:

$$\bar{\mathbf{x}} = \mathbf{x}_{\text{eq}} + \boldsymbol{\varepsilon} \quad (10)$$

By taking $\boldsymbol{\varepsilon} \rightarrow 0$, a Taylor expansion of the right side of the system is performed:

$$\mathbf{f}_{\text{NL}}(\mathbf{x}) = \mathbf{f}_{\text{NL}}(\mathbf{x}_{\text{eq}}) + \mathbf{J}_{\text{f}_{\text{NL}}}(\mathbf{x}_{\text{eq}})\boldsymbol{\varepsilon} + o(\boldsymbol{\varepsilon}) \quad (11)$$

$\mathbf{J}_{\text{f}_{\text{NL}}}(\mathbf{x}_{\text{eq}})$ is the Jacobian matrix of the nonlinear forces evaluated in \mathbf{x}_{eq} . Hence, by writing Eq. 1 for $\mathbf{x} = \bar{\mathbf{x}}$, the following expression is obtained:

$$\mathbf{M}\ddot{\boldsymbol{\varepsilon}} + \mathbf{C}\dot{\boldsymbol{\varepsilon}} + (\mathbf{K} - \mathbf{J}_{\text{f}_{\text{NL}}}(\mathbf{x}_{\text{eq}}))\boldsymbol{\varepsilon} = \mathbf{0} \quad (12)$$

The eigenvalues and eigenvectors of this system of equations provide the information on the eigenmodes of the mechanical system. A mode is defined as unstable if the real part of the associated eigenvalue is positive.

2.4 Contact expressions

In this section, the analytical expressions of contact used in the article are described. A penalty algorithm is used: this requires to define a contact stiffness k and to calculate the distance between two disks in contact, in order to obtain the normal and tangent forces. Let us consider a point placed on the contact surface of a disk, defined by its polar coordinates (r, θ) . The normal and tangent forces are given by:

$$\begin{cases} \mathbf{f}_{\text{N}}(r, \theta) = kd(r, \theta)\vec{u}_z \\ \mathbf{f}_{\text{T}}(r, \theta) = \mu kd(r, \theta)\vec{u}_\theta \end{cases} \quad (13)$$

where $d(r, \theta)$ is the gap between the point (r, θ) and the surface of the next disk.

2.4.1 Rigid disks model (integral formulation)

The rigid disks model is illustrated by Fig. 3a and b. Since the disks are considered to be rigid, every point of a disk can be described by the 6 DoF of its center. Displacements are assumed to be small. For a given couple of disks, the relative displacement and rotation of their centers allow to write the distance $d(r, \theta)$ for every point of the contact surface as follows:

$$d(r, \theta) = d_z + r \sin \theta \alpha_x - r \cos \theta \alpha_y \quad (14)$$

Where d_z is the relative displacement over \vec{z} and α_x (respectively, α_y) is the relative rotation over \vec{x} (respectively, \vec{y}).

By an integration over the contact surface of a disk, an analytical expression of the corresponding forces (F_x, F_y, F_z) and moments (M_x, M_y, M_z) is obtained.

$$F_x^{\text{integral}} = - \int_0^{2\pi} \int_{R_i}^{R_e} f_T(r, \theta) \sin(\theta) r dr d\theta = -\frac{1}{3} \mu k_I \pi (R_e^3 - R_i^3) \alpha_x \quad (15)$$

$$F_y^{\text{integral}} = \int_0^{2\pi} \int_{R_i}^{R_e} f_T(r, \theta) \cos(\theta) r dr d\theta = -\frac{1}{3} \mu k_I \pi (R_e^3 - R_i^3) \alpha_y \quad (16)$$

$$F_z^{\text{integral}} = \int_0^{2\pi} \int_{R_i}^{R_e} f_N(r, \theta) r dr d\theta = k_I \pi (R_e^2 - R_i^2) d_z \quad (17)$$

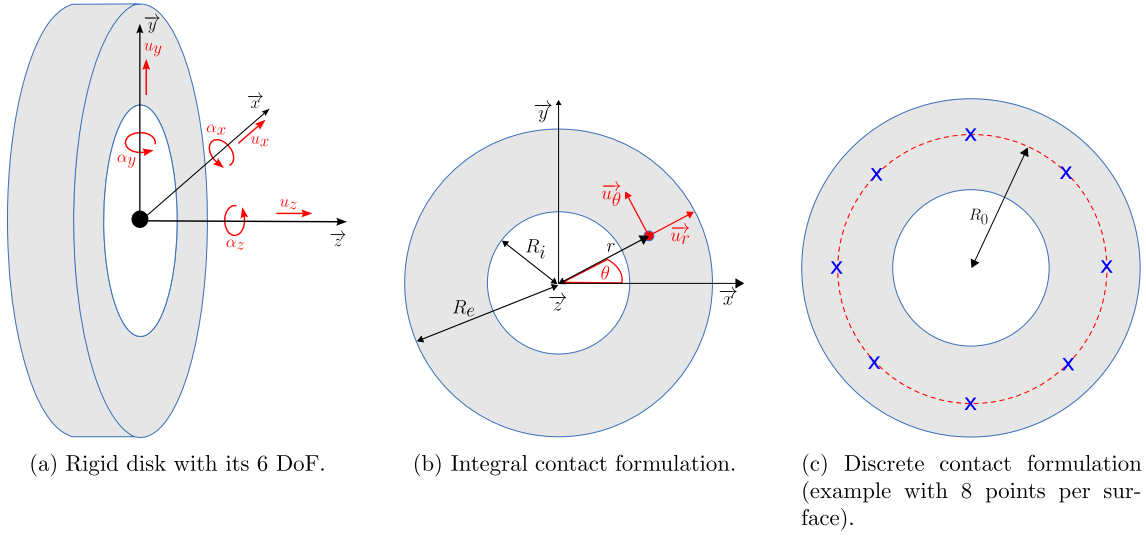


Fig. 3 Summary of the models used to represent the disks

$$M_x^{\text{integral}} = \int_0^{2\pi} \int_{R_i}^{R_e} f_N(r, \theta) \sin(\theta) r^2 dr d\theta = \frac{1}{4} k_I \pi (R_e^4 - R_i^4) \alpha_x \quad (18)$$

$$M_y^{\text{integral}} = - \int_0^{2\pi} \int_{R_i}^{R_e} f_N(r, \theta) \cos(\theta) r^2 dr d\theta = \frac{1}{4} k_I \pi (R_e^4 - R_i^4) \alpha_y \quad (19)$$

$$M_z^{\text{integral}} = \int_0^{2\pi} \int_{R_i}^{R_e} f_T(r, \theta) r^2 dr d\theta = \frac{2}{3} k_I \mu \pi (R_e^3 - R_i^3) d_z \quad (20)$$

k_I is the contact stiffness used for the integral formulation, R_i and R_e are the internal and external radii of the disks.

2.4.2 Non-rigid disks model (discrete formulation)

For the non-rigid disks model, the information about of the displacement of every point of the disk is individual and cannot be extracted from the DoF of the center. Hence, a fixed number N of points is chosen on the Finite Element model and the DoF of those points are retrieved. Figure 3c is an example where 8 points per contact surface are used. As a consequence, the axial distance $d(r, \theta)$ is only known for these points, which leads to a discrete expression for the disks contact.

$$d_i = z_{\text{rotor},i} - z_{\text{stator},i} \quad (21)$$

Replacing the integral formulation by the discrete one, the forces become:

$$F_x^{\text{discrete}} = \sum_{i=1}^N F_{x,i}^{\text{discrete}} = -\mu k_D \sum_{i=1}^N d_i \sin \theta_i \quad (22)$$

$$F_y^{\text{discrete}} = \sum_{i=1}^N F_{y,i}^{\text{discrete}} = \mu k_D \sum_{i=1}^N d_i \cos \theta_i \quad (23)$$

$$F_z^{\text{discrete}} = \sum_{i=1}^N F_{z,i}^{\text{discrete}} = k_D \sum_{i=1}^N d_i \quad (24)$$

k_D is the contact stiffness used in the discrete formulation. The moments are obtained by using the fulcrum expression. For a given point, its moments are written:

$$M_i^{\text{discrete}} = \begin{pmatrix} F_{x,i}^{\text{discrete}} \\ F_{y,i}^{\text{discrete}} \\ F_{z,i}^{\text{discrete}} \end{pmatrix} \times \begin{pmatrix} r_i \cos \theta_i \\ r_i \sin \theta_i \\ 0 \end{pmatrix} \quad (25)$$

The total moments are obtained by summing the moments for each point.

2.5 Component mode synthesis

CMS is a general term describing reduction techniques aiming to decrease the number of DoF of a given model. In this paper a Finite Element model is used, which makes CMS techniques particularly suitable with respect to other existing techniques. First of all, they can be implemented directly from a FE model. Besides, the goal is to ensure the precision of the model until a limit frequency, and this is exactly what CMS techniques provide, as it will be shown in Sect. 3.4. The method introduced here aims to reduce the number of interface DoF and is well-adapted to the case of frictional contact. Let us consider the reduced model with non-rigid disks. The Craig-Bampton reduction and substructuring assembly have been applied. The vector \mathbf{u} contains every DoF issued from the model reduction. To simplify the expressions, the undamped linear system is considered in this example. The DoF vector is organized as follows:

$$\mathbf{u} = \begin{pmatrix} \mathbf{u}_0 \\ \mathbf{u}_i \end{pmatrix} \quad (26)$$

The vector \mathbf{u}_0 contains the DoF which will not be affected by the CMS. Here it corresponds to the physical DoF of the system, other than the ones in the disks, as well as the non-physical DoF remaining after the Craig-Bampton reduction. The vector \mathbf{u}_i contains the DoF of the disks interfaces and they are the ones that will be reduced in this step. The goal is to write the system equation in a new basis which dimension will be smaller than \mathbf{u} , while ensuring a satisfying precision on the eigenmodes estimation.

Using Eq. 26, the motion equation becomes:

$$\mathbf{M}\ddot{\mathbf{u}} + \mathbf{K}\mathbf{u} = \begin{pmatrix} \mathbf{M}_{00} & \mathbf{M}_{0i} \\ \mathbf{M}_{i0} & \mathbf{M}_{ii} \end{pmatrix} \begin{pmatrix} \ddot{\mathbf{u}}_0 \\ \ddot{\mathbf{u}}_i \end{pmatrix} + \begin{pmatrix} \mathbf{K}_{00} & \mathbf{K}_{0i} \\ \mathbf{K}_{i0} & \mathbf{K}_{ii} \end{pmatrix} \begin{pmatrix} \mathbf{u}_0 \\ \mathbf{u}_i \end{pmatrix} = \begin{pmatrix} \mathbf{0} \\ \mathbf{0} \end{pmatrix} \quad (27)$$

Modal synthesis consists of two steps. First, the modal basis of the interfaces is truncated in order to reduce the dimension of the reduced basis. If a non-null friction coefficient is considered, the matrix \mathbf{K}_{ii} is non-symmetric, so the right and left eigenvectors need to be separated.

$$(\mathbf{K}_{ii}(\mu_{\text{CMS}}) - \omega^2 \mathbf{M}_{ii}) \boldsymbol{\phi}_r = \mathbf{0} \quad (28)$$

$$\boldsymbol{\phi}_l^T (\mathbf{K}_{ii}(\mu_{\text{CMS}}) - \omega^2 \mathbf{M}_{ii}) = \mathbf{0} \quad (29)$$

Once the eigenvectors $\boldsymbol{\phi}_r$ and $\boldsymbol{\phi}_l$ are obtained, the modal basis is sorted in the ascending order of its eigenfrequencies and the truncation is realized at the n^{th} mode. The truncated left (respectively, right) modal basis is written $\mathbf{V}_{l,n}$ (respectively, $\mathbf{V}_{r,n}$) and the related vector is written \mathbf{u}_n .

The second step of the CMS consists of solving the static problem. Let us write the second line of Eq. 27:

$$-\omega^2 \mathbf{M}_{i0} \ddot{\mathbf{u}}_0 - \omega^2 \mathbf{M}_{ii} \ddot{\mathbf{u}}_i + \mathbf{K}_{i0} \mathbf{u}_0 + \mathbf{K}_{ii} \mathbf{u}_i = \mathbf{0} \quad (30)$$

By considering the static solution, i.e., $\omega = 0$, the following relation is obtained:

$$\mathbf{u}_i = -\mathbf{K}_{ii}^{-1} \mathbf{K}_{i0} \mathbf{u}_0 \quad (31)$$

By combining Eqs. 28, 29 and 31, an expression of the transformation matrices associated to the modal synthesis are obtained.

$$\mathbf{T}_1 = \begin{pmatrix} \mathbf{I} & \mathbf{0} \\ -\mathbf{K}_{ii}^{-1} \mathbf{K}_{i0} & \mathbf{V}_{l,n} \end{pmatrix} \quad (32)$$

$$\mathbf{T}_r = \begin{pmatrix} \mathbf{I} & \mathbf{0} \\ -\mathbf{K}_{ii}^{-1} \mathbf{K}_{io} & \mathbf{V}_{r,n} \end{pmatrix} \quad (33)$$

After modal synthesis, Eq. 27 becomes:

$$\tilde{\mathbf{M}}\ddot{\tilde{\mathbf{u}}} + \tilde{\mathbf{K}}\tilde{\mathbf{u}} = 0 \quad (34)$$

Where

$$\tilde{\mathbf{M}} = \mathbf{T}_1^T \mathbf{M} \mathbf{T}_r \quad (35)$$

$$\tilde{\mathbf{K}} = \mathbf{T}_1^T \mathbf{K} \mathbf{T}_r \quad (36)$$

$$\tilde{\mathbf{u}} = \begin{pmatrix} \mathbf{u}_0 \\ \mathbf{u}_n \end{pmatrix} \quad (37)$$

The precision and the effectiveness of the modal synthesis are both regulated by the choice of n .

It is important to note that the friction coefficient μ_{CMS} used here can be different from the value used in the non-reduced stiffness matrix \mathbf{K} . This proves to be useful in the case $\mu_{\text{CMS}} = 0$. In this case, the right and left eigenvectors in Eqs. 32 and 33 are identical, which simplifies the equations and reduces the computations required to obtain the reduced system without making the distinction between left and right eigenvectors. Depending on the system under study, this assumption might have a meaningful impact on the precision [33].

3 Results

3.1 Coherence of the contact expressions

It is important to verify that the integral and discrete contact expressions are coherent with each other. In order to do so, the stiffness coefficients k_I and k_D need to be related. In the discrete formulation, the contact forces are simulated by a number N of axial springs. Hence, the total force can be calculated by considering N parallel spring of stiffness k_D . By dividing by the total surface of the disk, a stiffness per unit of surface is obtained.

$$k_D = \frac{\pi (R_e^2 - R_i^2)}{N} k_I \quad (38)$$

The forces and moments obtained for the integral and the discrete formulation can be compared for the rigid-disk case using the previous equations. If a discrete description of the rigid disks model is considered, Eq. 21 becomes:

$$d_i = d_z + r_i \sin \theta_i \alpha_x - r_i \cos \theta_i \alpha_y \quad (39)$$

As an example, the case where the points are distributed on a single radius is taken. R_0 will define such radius. By using Eqs. 22 to 25:

$$F_x^{\text{discrete}} = -\frac{1}{2} \pi \mu k_I R_0 (R_e^2 - R_i^2) \alpha_x \quad (40)$$

$$F_y^{\text{discrete}} = -\frac{1}{2} \pi \mu k_I R_0 (R_e^2 - R_i^2) \alpha_y \quad (41)$$

$$F_z^{\text{discrete}} = \pi k_I (R_e^2 - R_i^2) d_z \quad (42)$$

$$M_x^{\text{discrete}} = \frac{1}{2} \pi k_I R_0^2 (R_e^2 - R_i^2) \alpha_x \quad (43)$$

$$M_y^{\text{discrete}} = \frac{1}{2} \pi k_I R_0^2 (R_e^2 - R_i^2) \alpha_y \quad (44)$$

$$M_z^{\text{discrete}} = \pi \mu k_I R_0 (R_e^2 - R_i^2) d_z \quad (45)$$

When the expressions are compared using Eq. 38, two ratios appear. The first one is:

$$\eta_1 = \frac{F_x^{\text{integral}}}{F_x^{\text{discrete}}} = \frac{F_y^{\text{integral}}}{F_y^{\text{discrete}}} = \frac{M_z^{\text{integral}}}{M_z^{\text{discrete}}} = \frac{2}{3} \frac{R_e}{R_0} \left(\frac{1 - (\frac{R_i}{R_e})^3}{1 - (\frac{R_i}{R_e})^2} \right) \quad (46)$$

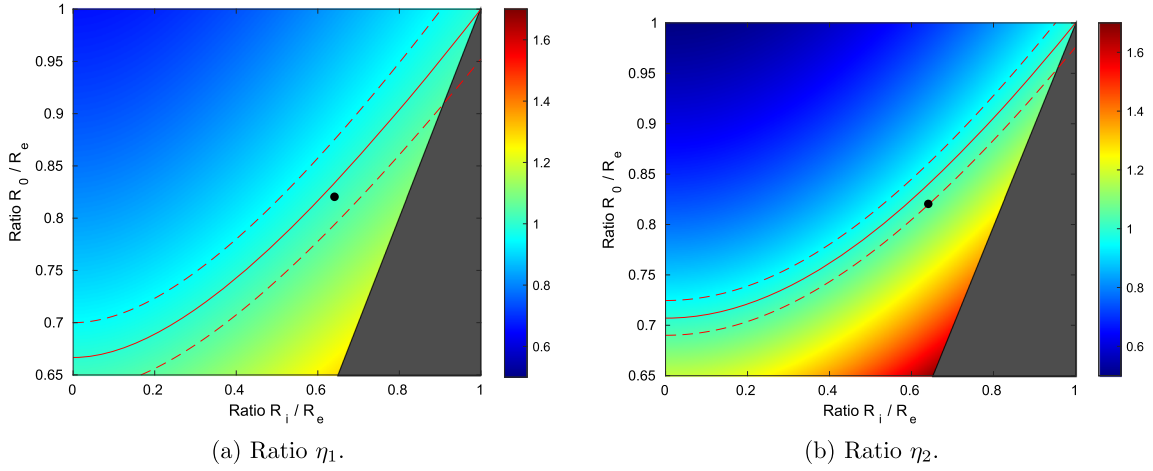


Fig. 4 Values of the ratios depending on the dimensions of the disks. The solid line is the function $\eta = 1$, the dashed lines surround the $\pm 5\%$ zone. The black dot is the ratio obtained with the parameters used in the model

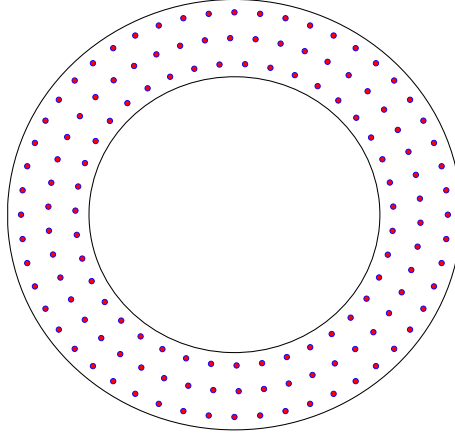


Fig. 5 Reference model with contact points distributed along three radii

It is the ratio for the in-plane forces F_x , F_y and the axial moment M_z . The second one is:

$$\eta_2 = \frac{M_x^{\text{integral}}}{M_x^{\text{discrete}}} = \frac{M_y^{\text{integral}}}{M_y^{\text{discrete}}} = \frac{1}{2} \frac{R_e^2}{R_0^2} \left(\frac{1 - (\frac{R_i}{R_e})^4}{1 - (\frac{R_i}{R_e})^2} \right) \quad (47)$$

It is the ratio for the in-plane moments M_x , M_y . The ratio of the axial forces F_z is equal to 1 because of Eq. 38.

Figure 4 shows the values of ratios η_1 and η_2 depending on R_e , R_i and R_0 . It is interesting to see that for a given dimension ratio for the disks, R_0 can be chosen to have one of the two ratios equal to 1, but not both (the only exception being the degenerate case $R_i = R_e$). For the paper, the radius R_0 was chosen to be halfway between the internal and external radii, which leads to errors around 2% for η_1 and 5% for η_2 .

This comparison allows to check that both formulations give similar results in the rigid disks case and it allows to estimate the discretization error depending on the extraction points.

3.2 Choice of point distribution

When considering a non-rigid disks model, the number and place of the contact points affect the results provided by the model. It is then fundamental to ensure that the choice of points will not introduce an important error on the stability analysis for the frequency range of interest. At the same time, a high amount of points

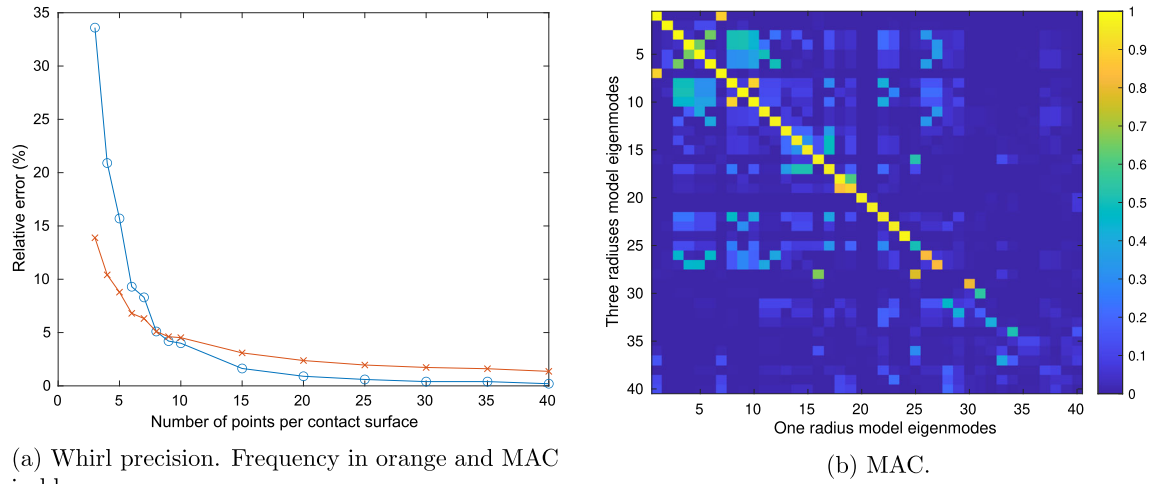


Fig. 6 Convergence of the non-rigid model with respect to the reference model, as a function of the number of points per contact surface

per surface of contact will increase the computation time, so a compromise has to be found. A convergence study has been performed in order to verify the minimum amount of points required to ensure the precision of the results. A reference model was considered, with contact points distributed along three radii. Such discrete distribution showed to give consistent results with respect to the Finite Element model, which is why it is considered as a reference model. The example of one contact surface is given in Fig. 5. This model contains around 7000 DoF, 10 times more than the rigid disks model. The stability analysis is performed and then its results are compared to a model containing between 3 and 40 points per contact surface, distributed on a single radius (the example for 8 points is provided in Fig. 3c). The convergence of the model is quantified through the whirl eigenfrequency and through the MAC (Modal Assurance Criterion). The MAC is a correlation criterion between two families of vectors. For two given vectors \mathbf{x} and \mathbf{y} , their MAC is calculated as follows:

$$\text{MAC}(\mathbf{x}, \mathbf{y}) = \frac{|\langle \mathbf{x}, \mathbf{y}^* \rangle|^2}{\langle \mathbf{x}, \mathbf{x}^* \rangle \langle \mathbf{y}, \mathbf{y}^* \rangle} \quad (48)$$

where \mathbf{x}^* indicates the conjugate of \mathbf{x} and $\langle \cdot, \cdot \rangle$ the scalar product of two vectors. If the mode shapes are identical, the MAC will have a value of 1. For modes with different shapes, the MAC is less than 1, a MAC value close to 0 indicating that the mode shapes are very different. When two models are compared, their eigenmodes are sorted by frequency: in the case of a couple of complex eigenmodes, the unstable mode (i.e., the one with a positive real part) is put before the stable one (i.e., the one with a negative real part).

The results are illustrated by Fig. 6. Convergence is observed for both indicators, the MAC having a faster convergence than the eigenfrequency. In order to compare the 40 points model to the reference model, the MAC for the first 40 eigenmodes is displayed in Fig. 6b. The whirl eigenmodes are number 10 and 11, so the one-radius model is considered to be an accurate representation of the non-rigid disks model as far as whirl is concerned. For the rest of the article, every time the non-rigid model is mentioned, it will be the one-radius model with 40 points per contact surface. It contains around 2700 DoF.

3.3 Stability analysis without CMS

This section is dedicated to comparing the stability results depending on whether disks deformation is considered. In this paper, three characteristics are monitored in order to assess the precision of each model: the eigenfrequency of the unstable whirl mode, its real part and the eigenvectors (through the MAC). The MAC is calculated based on the DoF shared by the two models. The DoF used for applying the contact laws are not taken into account. Here the rigid disks model and the 40-points non-rigid disks model are compared. First of all, stability analyses are carried out for the case $\mu = 0$ (see Fig. 7) and for the case $\mu > \mu_c$ (see Fig. 8). μ_c is the critical friction coefficient and indicates the friction coefficient for which the real part of whirl becomes positive. Such definition entails that every unstable mode is associated to a different value of μ_c . As far as whirl

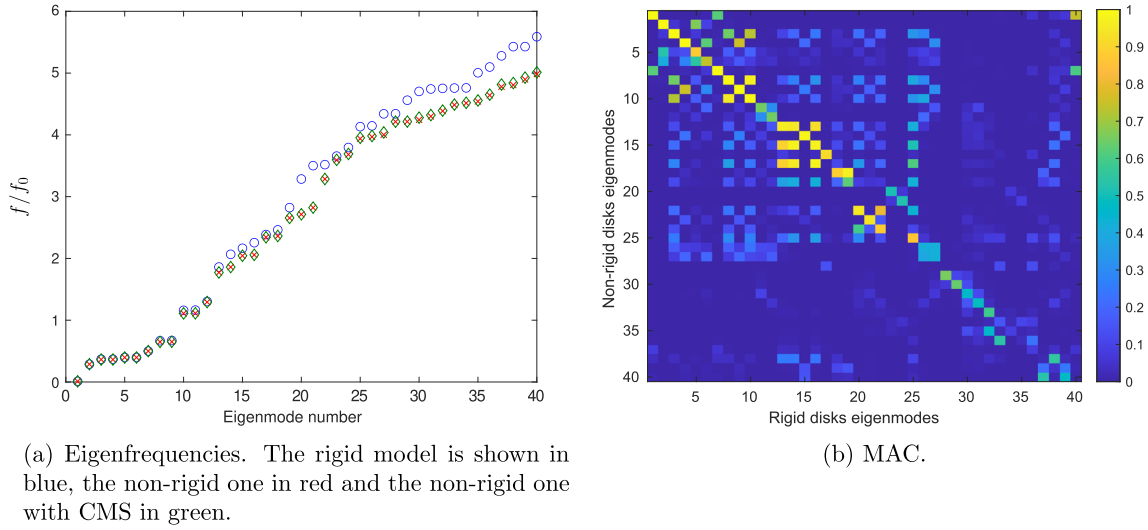


Fig. 7 Comparison of the rigid model and the non-rigid one for $\mu = 0$

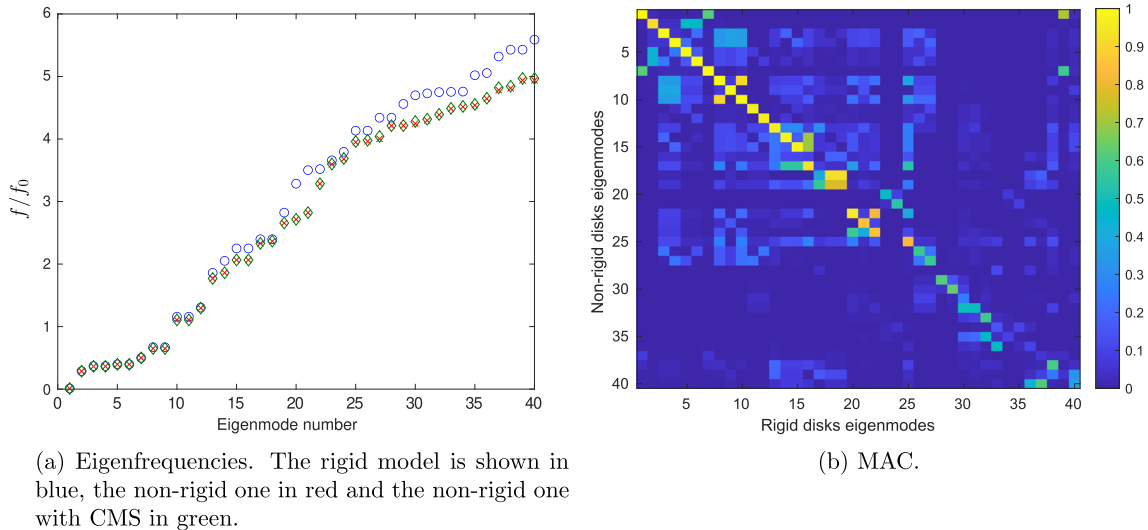


Fig. 8 Comparison of the rigid model and the non-rigid one for $\mu > \mu_c$

is concerned, it is equal to 0.14 for the rigid-disk model. The whirl eigenmodes are number 10 and 11. In both cases, the MAC shows that the first eigenmodes are very similar, the main exception being the stable whirl eigenmodes obtained in Fig. 7a. The lower value for the MAC can be explained by observing the shape of the eigenmodes. For $\mu = 0$, no coupling is present, so the two eigenmodes consist of one horizontal oscillation and one vertical oscillation. An illustration of the eigenmodes is provided in Annex A. Those eigenmodes are present in both models, but with an angular shift θ .

The value of θ can be linked to the fairly low value of the MAC observed for this couple of eigenmodes. As an example, let us consider two vectors \mathbf{x}_1 and \mathbf{x}_2 . \mathbf{x}_2 is obtained by rotating \mathbf{x}_1 of an angle θ .

$$\mathbf{x}_1 = \begin{pmatrix} x_0 \\ y_0 \end{pmatrix} \quad \mathbf{x}_2 = \begin{pmatrix} x_0 \cos \theta + y_0 \sin \theta \\ y_0 \cos \theta - x_0 \sin \theta \end{pmatrix} \quad (49)$$

By applying Eq. 48, we obtain:

$$\text{MAC}(\mathbf{x}_1, \mathbf{x}_2) = \cos^2 \theta \quad (50)$$

Once the coalescence is obtained (see Fig. 8b), such shift is no longer present. From the MAC pictures, it can be observed that the deformation of the disks has an influence starting with the 15th mode, which is located

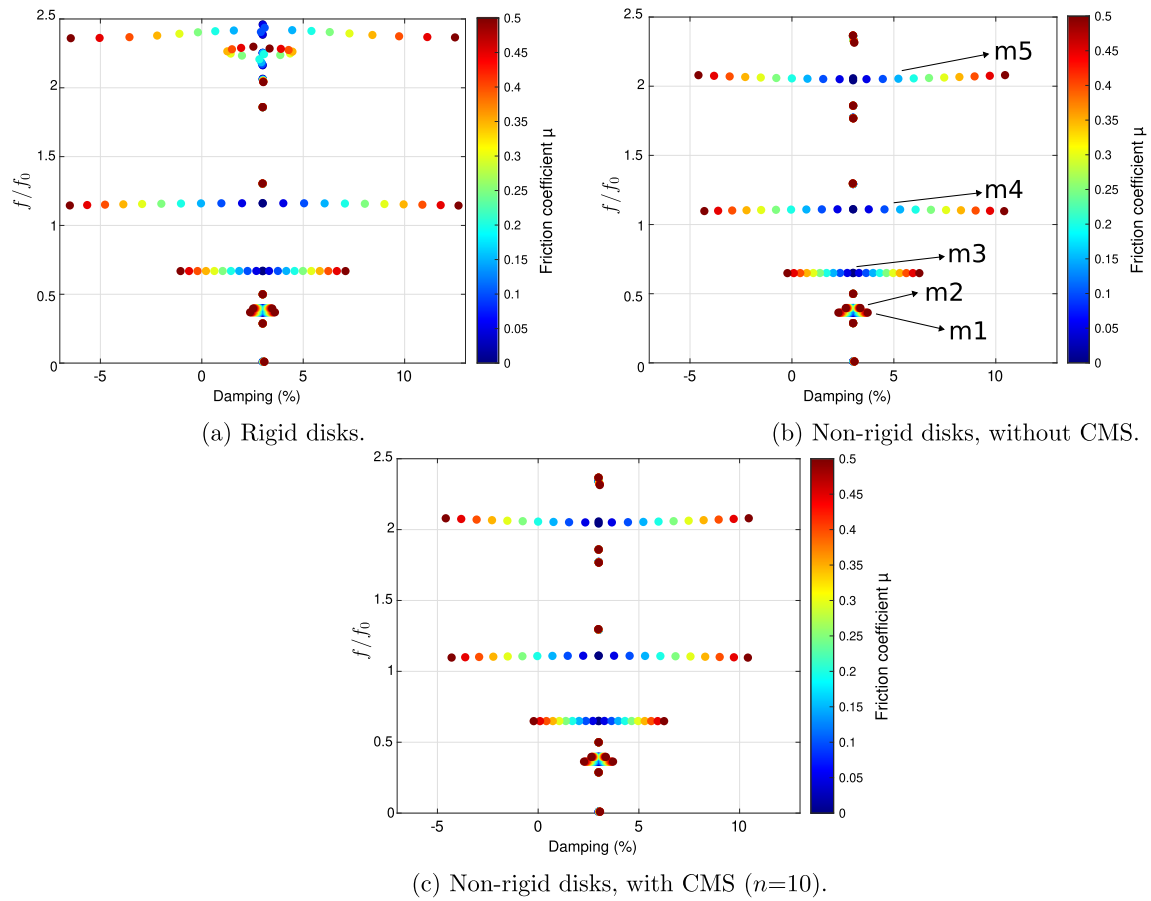


Fig. 9 Comparison of the stability charts

at around $2f_0$ (f_0 being the whirl eigenfrequency for the reference model). For the whirl eigenmodes, an error equal to 2.0% on the MAC and equal to 5.5% on the frequency is obtained. In order to take into account the real part of the unstable eigenmodes, the stability chart is plotted for the models (see Fig. 9).

Five mode couplings can be observed for the non-rigid disks model in the frequency range of interest. Figure 9b gives the notation used for those eigenmodes. The lowest frequency one, m1, consists in the oscillation of the whole brake following the deflection of the axle. The brake and the tire move in phase. m2 is essentially a displacement of the tire, while m3 is very similar to m1, but the brake and the tire move in opposition of phase. Whirl is designated by m4, and for m5 the displacement of the piston housing is similar to the one of whirl, but the axle moves as a rigid body (see Annex A).

Regarding the critical friction coefficient μ_c , the value estimated with the non-rigid disks model is equal to 0.20, a value 33% higher than the one obtained with the rigid disks model. This highlights the importance of taking into account disks deformation. Such discrepancy in the real part estimation will lead to a different propensity and onset of the whirl depending on which model is used. At this stage it is important to remember that the stability analysis is only a first step for the design of aircraft braking system in regard to friction-induced vibrations. It is well-known that the stability analysis may lead to an over-estimation or an underestimation of the unstable modes observed in the real nonlinear vibration behavior due to the fact that linear conditions (i.e., the linearized stability around an initial equilibrium point) are not valid during transient oscillations [26].

In conclusion, the non-rigid disks model is more accurate regarding the prediction of stability analysis, but its main drawback is the increase in the number of DoF considered. The following part discusses the use of CMS to reduce the size of the model while keeping a satisfying precision.

3.4 Performance of the CMS

The CMS step introduced here is led by two parameters, as shown in Eqs. 28, 29, 32 and 33: the friction coefficient μ_{CMS} used to build the transformation matrices and the number of interface modes n . The performance of the CMS is defined as both the precision of the reduced model with respect to the reference, and the reduction of the number of DoF. The goal is to assess the influence of two CMS parameters on those performances, in order to select a fitting set of (n, μ_{CMS}) which will guarantee a good prediction of whirl.

In order to monitor the precision of the model after applying CMS, a relative error is defined for the first m eigenmodes:

$$\forall i \in [1, m], x_i = \frac{|f_i - f_{i,0}|}{f_{i,0}} \quad (51)$$

Where f_i indicates the i^{th} frequency of the model under study and $f_{i,0}$ the i^{th} frequency of the model without CMS. The same equation can be written for the real parts instead of the eigenfrequencies. It is then possible to obtain the mean error through the following equation:

$$\bar{x}(m) = \frac{1}{m} \sum_{i=1}^m x_i \quad (52)$$

Likewise, the standard deviation of the error is defined by:

$$\sigma(m) = \sqrt{\sum_{i=1}^m (x_i - \bar{x}(m))^2} \quad (53)$$

here the value $m = 40$ is chosen in order to cover the $[0; 5f_0]$ frequency range.

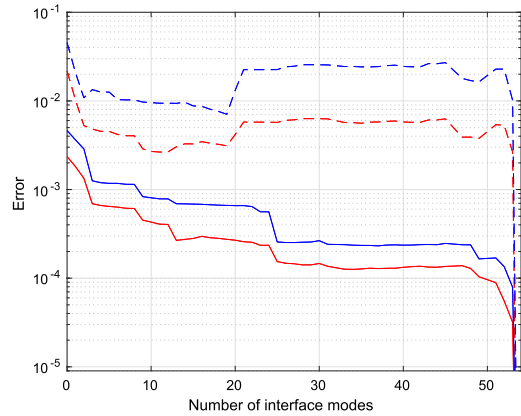
3.4.1 Rigid disks model

It is possible to apply the CMS method to the rigid disks model. If the rigidity hypothesis is considered to be satisfying, this proves to be useful in order to reduce the number of DoF of the model. Similarly to the non-rigid case, CMS is applied to the model with $\mu_{\text{CMS}} = 0$ and with n between 0 and the maximum number of DoF of interface. Since 9 disks are considered, $n_{\text{max}} = 54$. The results are given in Fig. 10 using the mean error and its standard deviation from Eqs. 52 and 53 for both eigenfrequencies and real parts. Figure 10a shows the convergence depending on the number of DoF. Results are similar to the non-rigid case, with a steep decrease of the mean error following the value of n . The standard deviation follows a different trend, increasing around $n = 20$. This indicates that the error decreases in a heterogeneous way among the eigenmodes under study. For the rigid-disk case, the situation $n = 0$, which corresponds to the Guyan reduction of the model [40], is already precise with respect to the reference model. Such reduction is then used in order to verify its performance and the stability chart is given in Fig. 10b. For $\mu = 0.3$, the error on whirl prediction is equal to 0.12% for the eigenfrequency and 3.20% for the real part. The model reduced with CMS is precise for whirl prediction and the number of DoF was decreased with respect to the reference model.

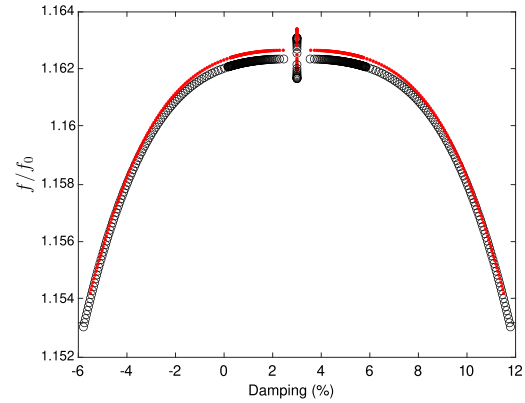
3.4.2 Non-rigid disks model

Here the reference model is the non-rigid disks model without CMS and with $\mu_0 = 0.3$. For the reduced model, 40 contact points are extracted from every contact surface, so n belongs in the range $[0; 1920]$.

First of all, the influence of n on the first eigenmodes is studied. In order to do so, CMS is applied for different values of n and the first eigenmodes are compared to the ones obtained without CMS, with respect to frequencies and real parts. The global result is shown in Fig. 11. As far as the frequencies are concerned, the error function is monotonous and decreasing. The same conclusion cannot be applied to the real parts, for which the error increases in some ranges of n . The evolution of the error for each eigenmode is given in Fig. 12. It can be seen that the error is generally more important on the high-frequency eigenmodes. Besides, the convergence speed is not the same for every eigenmode: for instance, Fig. 12a shows that the couple 26–27 has a frequency error higher than its neighbors for $n = 100$. These modes involve the ovalization of the disks,

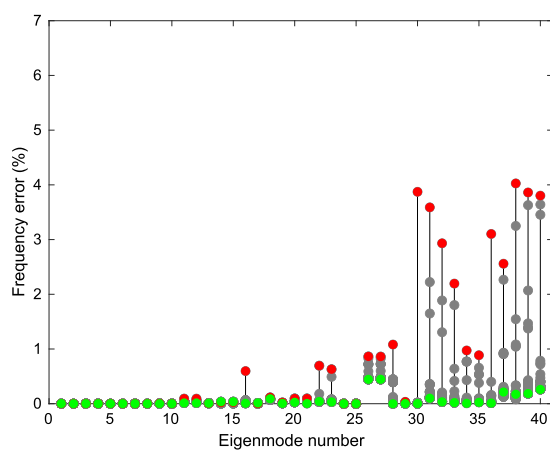


(a) Mean error (full lines) and standard deviation of the error (dotted lines) for frequencies (red) and real parts (blue) on the first 40 eigenmodes depending on the number of DoF ($\mu_0 = 0.3$ and $\mu_{CMS} = 0$).

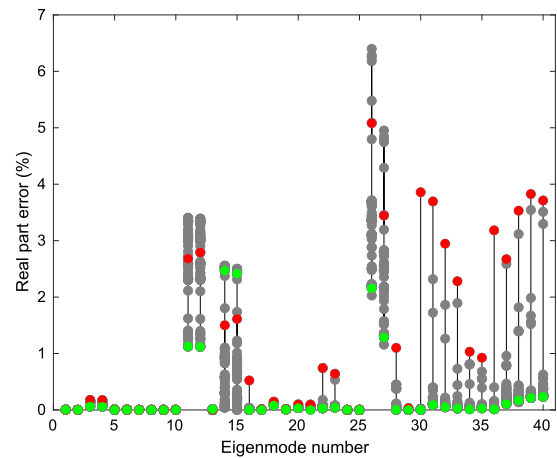


(b) Stability chart for whirl, considering the reference model (black) and the Guyan condensation (red) for μ varying from 0 to 0.5.

Fig. 10 CMS applied to the rigid disks model



(a) Eigenfrequencies.



(b) Real parts.

Fig. 11 Precision of the model on its first 40 eigenmodes using CMS. The red dots shows the error for $n = 0$, the green dots for $n = 100$ and the gray ones for the intermediate values of n . Calculations carried out for $\mu = 0.3$

hence they would not appear in the rigid disks model. Regarding real parts, it is interesting to note that the couple 14–15 (m5 in Fig. 9b) has a higher error for $n = 100$ than for $n = 0$.

Another important step is to evaluate the influence of μ_{CMS} on the precision of the reduced model. In particular, the case $\mu_{CMS} = 0$ needs to be investigated for the reasons mentioned in Sect. 2.5. Simulations are run for $\mu = \mu_0$ in the non-reduced system, whereas μ_{CMS} varies between 0 (dark blue line) and 0.3 (red line). Figure 11 shows the results. It is important to note that the case $\mu_{CMS} = \mu_0$ does not lead to the highest precision, for both eigenfrequencies and real parts. Regarding the eigenfrequencies (see Fig. 11a), the error globally decreases with n , with a steep slope for $n < 20$. The value of μ_{CMS} has very little influence on the precision, regardless of the value of n . More significant differences are observed for the real parts in Fig. 11b: in particular, the error increases steeply around $n = 40$. Once again, the case $\mu_{CMS} = \mu_0$ is the one with the highest mean error. As mentioned previously, the case $\mu_{CMS} = 0$ is interesting for its computation time. Its results are compared more in detail with the ones provided by $\mu_{CMS} = \mu_0$ in Fig. 13. For this specific model and for the frequency range of interest, the two options show very limited differences, so $\mu_{CMS} = 0$ is chosen.

To ensure that the reduced model is precise with respect to the reference, the MAC is plotted in Fig. 14 for three values of n and for $\mu_{CMS} = 0$. It is observed that $n = 10$ improves the precision on the high-frequency eigenmodes with respect to $n = 0$, whereas an increase toward $n = 100$ has no significant effect. Besides,

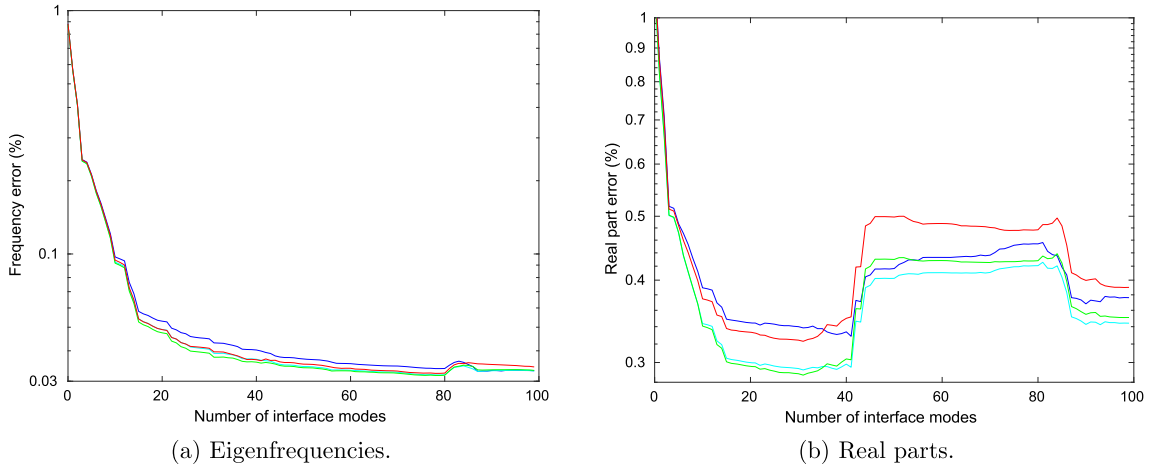


Fig. 12 Precision of the reduced model depending on the value of μ_{CMS} : $\mu_{CMS} = 0$ (blue), $\mu_{CMS} = 0.1$ (cyan), $\mu_{CMS} = 0.2$ (green) and $\mu_{CMS} = 0.3$ (red). Calculations carried out for $\mu = 0.3$

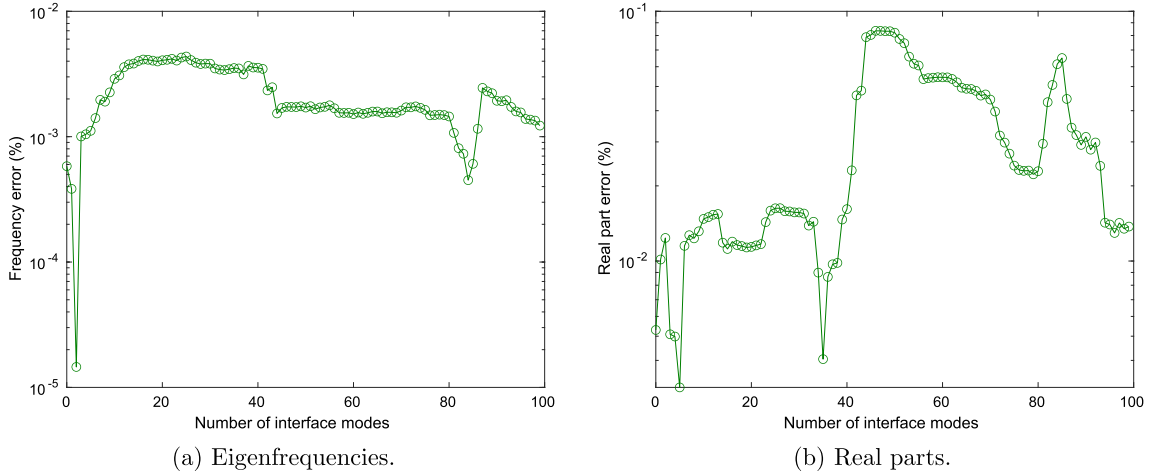


Fig. 13 Comparison of CMS results between $\mu_{CMS} = 0$ and $\mu_{CMS} = \mu_0$ on the first 40 eigenmodes, depending on the number of interface modes n . Calculations carried out for $\mu = 0.3$

every diagonal value in the MAC for $n = 10$ is higher than 99%. Hence, $n = 10$ is chosen as a satisfying compromise between model size and precision on the first eigenmodes of the system.

To summarize the main results of the study, the rigid model, the non-rigid one without CMS and the non-rigid one with CMS ($n = 10$, $\mu_{CMS} = 0$) are compared. The corresponding stability charts are shown in Fig. 9. It is seen that in order to ensure a proper estimation of the behavior of the reference model, while also reducing the number of DoF, CMS is a better alternative than considering rigid disks. It is interesting to note that, even though the transformation matrices for CMS are built using μ_{CMS} , the reduced matrices grant a satisfying precision in the friction coefficient range $[0; 0.3]$.

4 Conclusion

This paper aimed to compare the stability analysis for an aircraft braking system, depending on whether disks deformation is taken into account. It was found that eigenfrequencies and modal shapes are predicted in a similar way by both models, but there was an important discrepancy on the real part estimation. The rigid disks model over-estimates the instability of the system compared to the non-rigid disks model. This paper also introduced a CMS technique as a solution to reduce the size of the non-rigid disks model and allowed to determine an efficient reduction set considering both precision and model size. This allowed to obtain a non-rigid disks model with a number of DoF very similar to the rigid-disk model. This reduction method

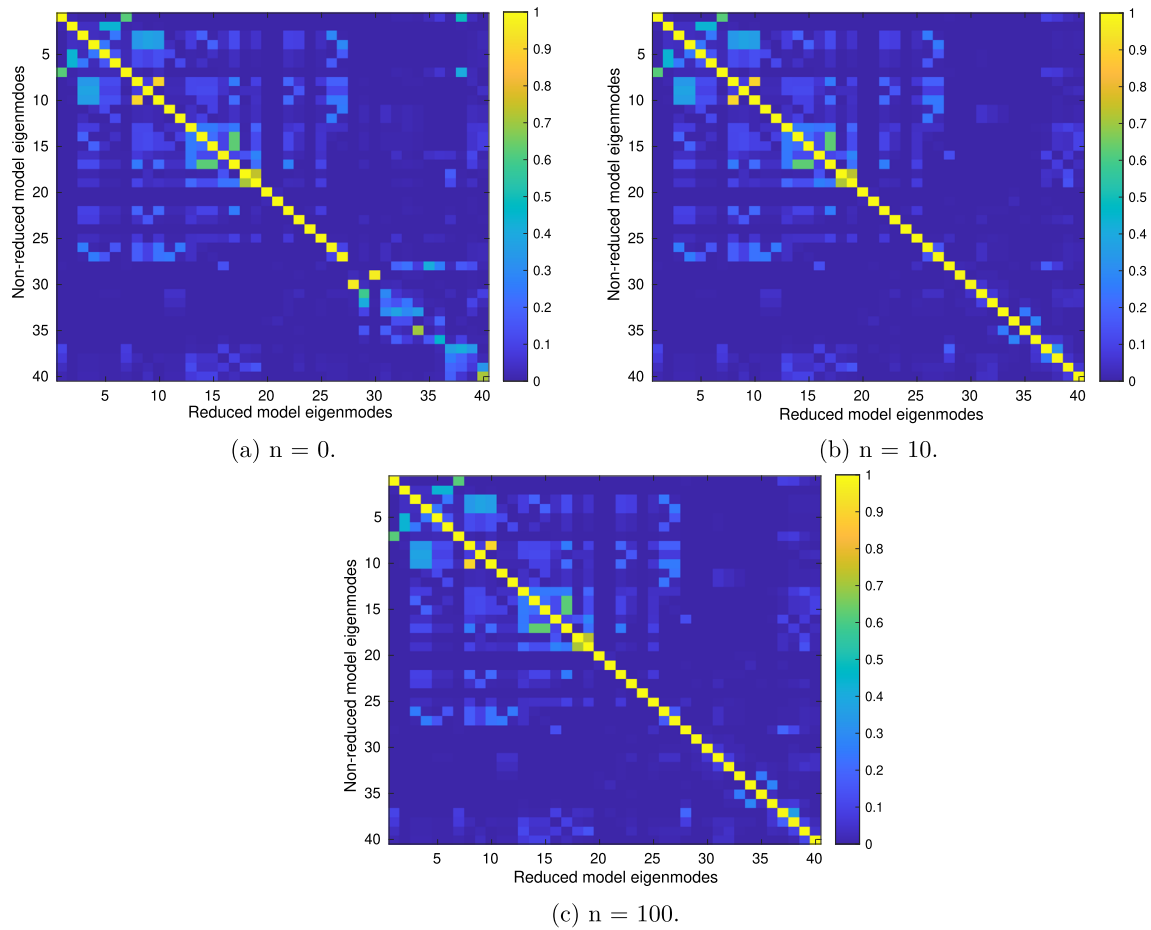


Fig. 14 Comparison of a few reduced models with respect to the reference model using MAC, calculations carried out for $\mu = 0.3$

showed to be well-suited to the system under study, because a very sharp reduction (very low value of n) and on a real basis ($\mu_{\text{CMS}} = 0$) proved to introduce a very limited error with respect to the non-reduced solution in the frequency range of interest.

These findings have an important effect for the development of aircraft braking systems. It was shown that, even though disks deformation does not play a significant role in the whirl eigenmode shape, it affects the real part of the mode, hence the propensity of the instability. In the paper, deformation reduces the real part and increases the critical friction coefficient, so a rigid disks model would over-estimate the instability propensity. This would lead to poor prediction of the onset of instability and thus of vibration performance for a given design, and it would lead to non-optimal design solution for aircraft safety.

Although it is not possible to draw up an exhaustive list of topics of interest for future developments, further studies relating to the prediction of friction-induced vibrations and transient nonlinear phenomena for aircraft braking systems, including disk deformations, would be essential to verify whether this leads to similar conclusions. Similarly, it could be interesting to compare in deep all the numerical results with experiments. On first analysis, it appears that the instability frequency predictions found in this study are in agreement with previously published experimental results [39]. However, it would be interesting to be able to carry out experimental studies demonstrating that disks deform during vibration. This would require the implementation of a complex experimental protocol and dedicated measurement resources. Finally, it would also be interesting to be able to propose technological solutions that would reduce or even eliminate these instability phenomena. This requires a sufficiently reliable numerical model to be able to implement a robust and well-managed design strategy.

Annex A: illustrations of the eigenmodes

Figures 15 and 16 illustrate the whirl unstable mode and the physical interactions between the elements of the aircraft brake system (with the wobbling motion of piston housing as well as the rotors and stators). The eigenmodes are illustrated through the displacement of the heatsink, the axle and the piston housing on the FE model. For the interested reader, Figs. 17 and 18 show the two initial stable modes at $\mu = 0$ that contribute to the whirl mode coupling at $\mu = \mu_c$. Finally Fig. 19 shows the high-frequency unstable mode denoted m5.

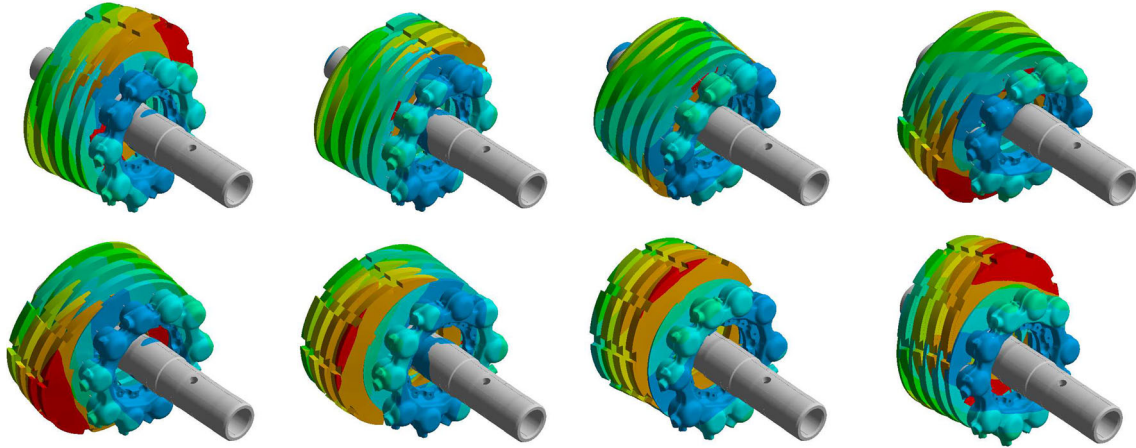


Fig. 15 Whirl eigenmode, isometric view

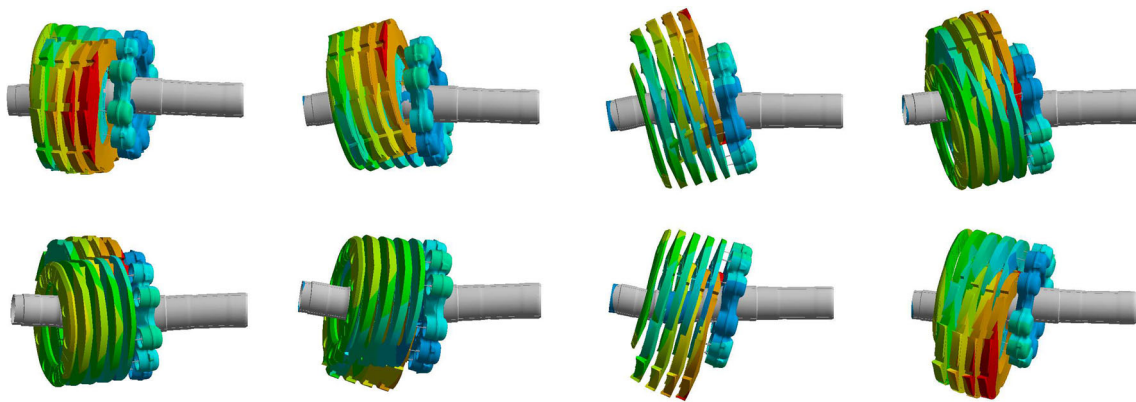


Fig. 16 Whirl eigenmode, top view

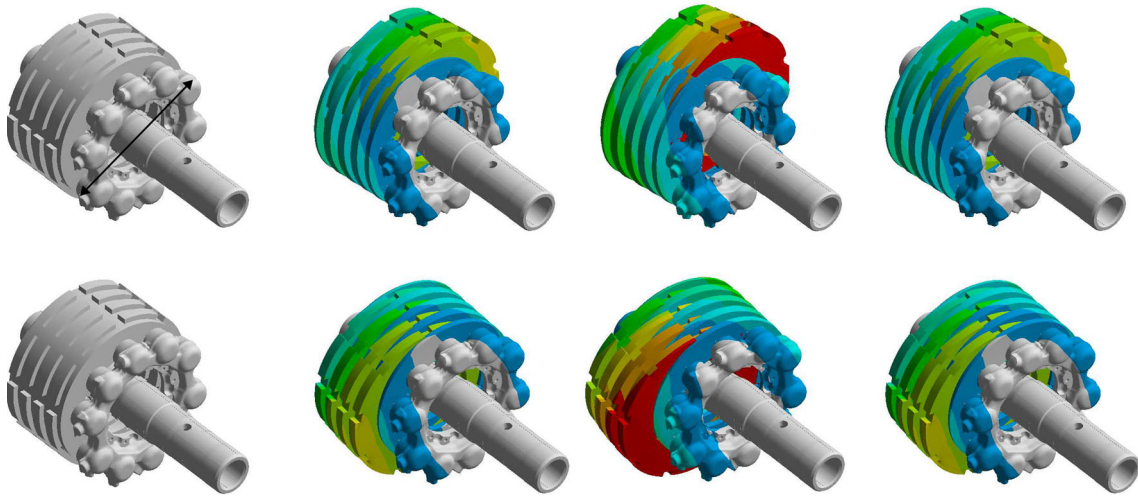


Fig. 17 Horizontal eigenmode for $\mu = 0$, isometric view

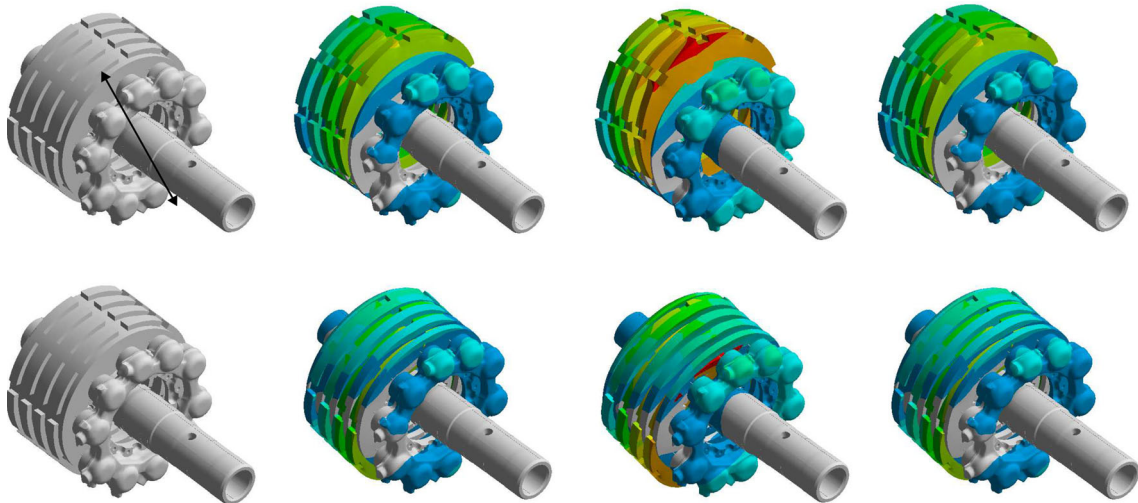


Fig. 18 Vertical eigenmode for $\mu = 0$, isometric view

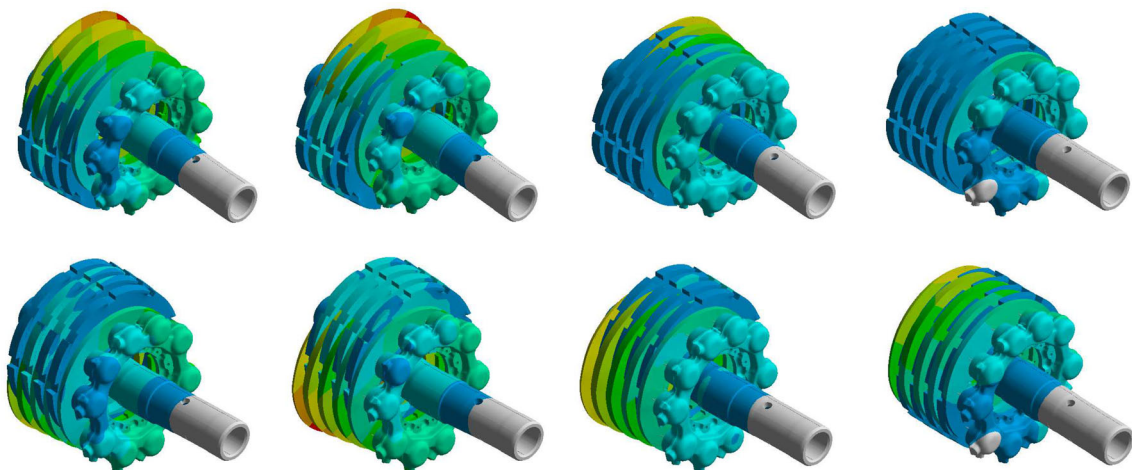


Fig. 19 High-frequency unstable mode, isometric view (denoted m5 in Fig. 9b)

Author contribution Conceptualization: X.F, J-J. S., S. B., L.J. and A. H.; Investigation: X.F, J-J. S., S. B., L.J. and A. H.; Methodology: X.F, J-J. S., S. B., L.J. and A. H.; Validation: X.F, J-J. S., S. B., L.J. and A. H.; Visualization: X.F; Writing original draft: X.F, J-J. S., S. B.; Writing review and editing: X.F, J-J. S., S. B.

Data Availability No datasets were generated or analysed during the current study.

Declarations

Conflict of interest The authors declare no competing interests.

Open Access This article is licensed under a Creative Commons Attribution-NonCommercial-NoDerivatives 4.0 International License, which permits any non-commercial use, sharing, distribution and reproduction in any medium or format, as long as you give appropriate credit to the original author(s) and the source, provide a link to the Creative Commons licence, and indicate if you modified the licensed material. You do not have permission under this licence to share adapted material derived from this article or parts of it. The images or other third party material in this article are included in the article's Creative Commons licence, unless indicated otherwise in a credit line to the material. If material is not included in the article's Creative Commons licence and your intended use is not permitted by statutory regulation or exceeds the permitted use, you will need to obtain permission directly from the copyright holder. To view a copy of this licence, visit <http://creativecommons.org/licenses/by-nc-nd/4.0/>.

References

1. Redfield, R.C.: Brake induced vibration in mountain bikes. *Eng. Sport* **7**, 587–596 (2008)
2. Kinkaid, N.M., O'Reilly, O.M., Papadopoulos, P.: Automotive disc brake squeal. *J. Sound Vib.* **267**(1), 105–166 (2003)
3. Ouyang, H., Nack, W., Yuan, Y., Chen, F.: Numerical analysis of automotive disc brake squeal: a review. *Int. J. Veh. Noise Vib.* **1**(3–4), 207–231 (2005)
4. Oberst, S., Lai, J.C.S., Marburg, S.: Guidelines for numerical vibration and acoustic analysis of disc brake squeal using simple models of brake systems. *J. Sound Vib.* **332**, 2284–2299 (2013)
5. Denimal, E., Sinou, J.-J., Nacivet, S.: Influence of structural modifications of automotive brake systems for squeal events with kriging meta-modelling method. *J. Sound Vib.* **463**, 114938 (2019)
6. Berndt, P.J., Schweiger, W.: Experimental and theoretical investigation of brake squeal with disc brakes installed in rail vehicles. *Wear* **113**(1), 131–142 (1986)
7. Lorang, X., Chiello, O.: Stability and transient analysis in the modeling of railway disc brake squeal. *Notes Numer. Fluid Mech. Multidiscip. Des.* **99**, 447–453 (2008)
8. Lorang, X., Foy-Margiocchi, F., Nguyen, Q.S., Gautier, P.E.: Tgv disc brake squeal. *J. Sound Vib.* **293**, 735–746 (2006)
9. Sinou, J.-J., Loyer, A., Chiello, O., Mogenier, G., Lorang, X., Cochetoux, F., Bellaj, S.: A global strategy based on experiments and simulations for squeal prediction on industrial railway brakes. *J. Sound Vib.* **332**, 5068–5085 (2013)
10. Tison, T., Heussaff, A., Massa, F., Turpin, I., Nunes, R.F.: Improvement in the predictivity of squeal simulations: uncertainty and robustness. *J. Sound Vib.* **333**, 3394–3412 (2014)
11. Nobari, A., Ouyang, H., Bannister, P.: Uncertainty quantification of squeal instability via surrogate modelling. *Mech. Syst. Signal Process.* **60–61**, 887–908 (2015)
12. Charroyer, L., Chiello, O., Sinou, J.J.: Estimation of self-sustained vibration for a finite element brake model based on the shooting method with a reduced basis approximation of initial conditions. *J. Sound Vib.* **468**, 115050 (2020)
13. Lai, V.V., Anciant, M., Chiello, O., Brunel, J.F., Duffrénoy, P.: A nonlinear FE model for wheel/rail curve squeal in the time-domain including acoustic predictions. *Appl. Acoust.* **179**, 108031 (2021)
14. Chevillat, F., Sinou, J.-J., Hardouin, N.: Nonlinear transient vibrations and coexistences of multi-instabilities induced by friction in an aircraft braking system. *J. Sound Vib.* **328**, 555–574 (2009)
15. Chevillat, F., Sinou, J.J., Hardouin, N., Jezequel, L.: Simulations and experiments of a nonlinear aircraft braking system with physical dispersion. *J. Vib. Acoust.* **132**, 11 (2010)
16. Meehan, P.A., Leslie, A.C.: On the mechanisms, growth, amplitude and mitigation of brake squeal noise. *Mech. Syst. Signal Process.* **152**, 107469 (2021)
17. Kim, C., Kwon, Y., Kim, D.: Analysis of low-frequency squeal in automotive disc brake by optimizing groove and caliper shapes. *Int. J. Precis. Eng. Manuf.* **19**(4), 505–512 (2018)
18. Noël, J.P., Kerschen, G.: Nonlinear system identification in structural dynamics: 10 more years of progress. *Mech. Syst. Signal Process.* **83**, 2–35 (2017)
19. Elmaian, A., Gautier, F., Pezerat, C., Duffal, J.M.: How can automotive friction-induced noises be related to physical mechanisms? *Appl. Acoust.* **76**, 391–401 (2014)
20. Crolla, D.A., Lang, A.M.: Brake noise and vibration-state of the art. *Tribol. Ser.* **18**, 165–174 (1991)
21. Papinniemi, A., Lai, J.C.S., Zhao, J., Loader, L.: Brake squeal: a literature review. *Appl. Acoust.* **63**, 391–400 (2002)
22. Ibrahim, R.A.: Friction-induced vibration, chatter, squeal and chaos part I: mechanics of contact and friction. *Appl. Mech. Rev.* **47**, 209–226 (1994)
23. Ibrahim, R.A.: Friction-induced vibration, chatter, squeal, and chaos-part ii: dynamics and modeling. *Appl. Mech. Rev.* **47**(7), 227–253 (1994)
24. Yoon, J., Park, J., Min, S.: Optimal disc brake design for reducing squeal instability using slip-dependent complex eigenvalue analysis. *Mech. Syst. Signal Process.* **177**, 109240 (2022)
25. Liu, N., Ouyang, H.: Friction-induced vibration considering multiple types of nonlinearities. *Nonlinear Dyn.* **102**(4), 2057–2075 (2020)

26. Sinou, J.J.: Transient non-linear dynamic analysis of automotive disc brake squeal - On the need to consider both stability and non-linear analysis. *Mech. Res. Commun.* **37**, 96–105 (2010)
27. Coudeyras, N., Sinou, J.-J., Nacivet, S.: A new treatment for predicting the self-excited vibrations of nonlinear systems with frictional interfaces: the constrained harmonic balance method, with application to disc brake squeal. *J. Sound Vib.* **319**(3–5), 1175–1199 (2009)
28. Oberst, S., Lai, J.C.S.: Nonlinear transient and chaotic interactions in disc brake squeal. (2015)
29. Craig, R.R., Bampton, M.C.C.: Coupling of substructures for dynamic analyses. *AIAA J.* **6**(7), 1313–1319 (1968)
30. MacNeal, R.H.: A hybrid method of component mode synthesis. *Comput. Struct.* **1**(4), 581–601 (1971)
31. Scheffold, D., Bach, C., Duddeck, F., Müller, G., Buchschmid, M.: Vibration frequency optimization of jointed structures with contact nonlinearities using hyper-reduction. *IFAC-PapersOnLine* **51**(2), 843–848 (2018)
32. Corradi, G., Sinou, J.J., Besset, S.: Performances of the double modal synthesis for the prediction of the transient self-sustained vibration and squeal noise. *Appl. Acoust.* **175**, 107807 (2021)
33. Besset, S., Sinou, J.J.: Modal reduction of brake squeal systems using complex interface modes. *Mech. Syst. Signal Process.* **85**, 896–911 (2017)
34. Wagner, A., Spelsberg-Korspeter, G., Hagedorn, P.: Structural optimization of an asymmetric automotive brake disc with cooling channels to avoid squeal. *J. Sound Vib.* **333**(7), 1888–1898 (2014)
35. Mercier, A., Jézéquel, L.: Influence of imperfections on the stability of a multi-disc friction system. *J. Sound Vib.* **524**, 116712 (2022)
36. Liu, N., Ouyang, H.: Friction-induced planar vibration of two rigid plates. *Appl. Math. Model.* **109**, 613–628 (2022)
37. Halloran, J.P., Easley, S.K., Petrella, A.J., Rullkoetter, P.J.: Comparison of deformable and elastic foundation finite element simulations for predicting knee replacement mechanics. *J. Biomech. Eng.* **127**(5), 813–818 (2005)
38. Giudice, J.S., Caudillo, A., Mukherjee, S., Kong, K., Park, G., Kent, R., Panzer, M.B.: Finite element model of a deformable American football helmet under impact. *Ann. Biomed. Eng.* **48**(5), 1524–1539 (2020)
39. Sinou, J.J., Dereure, O., Mazet, G.B., Thouverez, F., Jezequel, L.: Friction-induced vibration for an aircraft brake system-Part 1: experimental approach and stability analysis. *Int. J. Mech. Sci.* **48**(5), 536–554 (2006)
40. Guyan, R.: Reduction of stiffness and mass matrices. *AIAA J.* **3**(2), 380–380 (1965)

Publisher's Note Springer Nature remains neutral with regard to jurisdictional claims in published maps and institutional affiliations.